

**Title: A sea change in our view of overturning– first results from the
Overturning in the Subpolar North Atlantic Program**

Authors: M.S. Lozier^{1*}, F. Li^{1*}, S. Bacon², F. Bahr³, A.S. Bower³, S.A. Cunningham⁴, M.F. de Jong⁵, L. de Steur^{5‡}, B. deYoung⁶, J. Fischer⁷, S.F. Gary⁴, B.J.W. Greenan⁸, N.P. Holliday², A. Houk⁹, L. Houpert⁴, M.E. Inall⁴, W.E. Johns⁹, H.L. Johnson¹⁰, C. Johnson⁴, J. Karstensen⁷, G. Koman⁹, I.A. Le Bras¹¹, X. Lin¹², N. Mackay^{13†}, D.P. Marshall¹⁰, H. Mercier¹⁴, M. Oltmanns⁷, R.S. Pickart³, A.L. Ramsey³, D. Rayner², F. Straneo¹¹, V. Thierry¹⁵, D.J. Torres³, R.G. Williams¹⁶, C. Wilson¹³, J. Yang³, I. Yashayaev⁸, J. Zhao^{3&}

Affiliations:

¹ Duke University, Durham, North Carolina, USA.

² National Oceanography Centre, Southampton, UK.

³ Woods Hole Oceanographic Institution, Woods Hole, Massachusetts, USA.

⁴ Scottish Association for Marine Science, Oban, UK.

⁵ Royal Netherlands Institute for Sea Research and Utrecht University, Texel, Netherlands.

⁶ Memorial University, St. John's, Newfoundland, Canada.

⁷ GEOMAR Helmholtz Centre for Ocean Research, Kiel, Germany.

⁸ Bedford Institute of Oceanography, Dartmouth, Nova Scotia, Canada.

⁹ University of Miami, Miami, Florida, USA.

¹⁰ University of Oxford, Oxford, UK.

¹¹ Scripps Institution of Oceanography, UCSD, La Jolla, California, USA.

¹² Physical Oceanography Laboratory/Institute for Advanced Ocean Studies, Ocean University of China and Qingdao National Laboratory for Marine Science and Technology, Qingdao, China.

¹³ National Oceanography Centre, Liverpool, UK.

¹⁴ CNRS, Laboratoire d'Océanographie Physique et Spatiale, Plouzané, France.

¹⁵ IFREMER, Laboratoire d'Océanographie Physique et Spatiale, Plouzané, France.

¹⁶ University of Liverpool, Liverpool, UK.

*Correspondence should be addressed to: mslozier@duke.edu (MSL); feili.li@duke.edu (FL)

‡Current address: Norwegian Polar Institute, Tromsø, Norway

†Current address: University of Exeter, Devon, UK

&Current address: University of Maryland Center for Environmental Science, Cambridge, Maryland, USA

Abstract: To provide an observational basis for IPCC projections of a slowing Atlantic Meridional Overturning Circulation (MOC) in the 21st century, the Overturning in the Subpolar North Atlantic Program (OSNAP) observing system was launched in the summer of 2014. The

first 21-month record reveals a highly variable overturning circulation responsible for the majority of the heat and freshwater transport across the OSNAP line. In a departure from the prevailing view that changes in deep water formation in the Labrador Sea dominate MOC variability, these results suggest that the conversion of warm, salty, shallow Atlantic waters into colder, fresher, deep waters that move southward in the Irminger and Iceland basins, is largely responsible for overturning and its variability in the subpolar basin.

One Sentence Summary: Transatlantic observations contradict the prevailing view that deep water mass changes in the Labrador Sea dominate overturning variability.

Main Text:

Paleoceanographers have long interpreted millennial scale climate variability in the context of ocean dynamics. Alternate periods of global cooling and warming have been attributed to variability in the ocean's meridional overturning circulation (MOC), brought about by changes in deep water production at high latitudes in the North Atlantic (1). A collection of studies (2) in the 1990s changed our perception of the time scale on which overturning variability could influence the climate. Synchronous changes recorded in ice sheets in Greenland and Antarctica revealed global atmospheric temperature disruptions on the scale of years to decades. In response to concerns about abrupt climate change raised by these studies, the U.K. and the U.S. deployed the RAPID Meridional Overturning Circulation and Heat Flux Array (RAPID-MOCHA) in 2004 at 26.5°N in the subtropical North Atlantic to provide the first continuous direct measure of the overturning (3). Data from this array revealed strong variability on all observed times scales, strikingly altering our view of the overturning circulation (4).

In the fourteen years since the RAPID-MOCHA array was deployed, modeling and observational studies have suggested that overturning variability is not coherent between the subtropical and subpolar latitudes on interannual to decadal scales (5-7). Furthermore, modeling studies have shown that interannual variability in the RAPID-MOCHA time series can be largely reproduced by wind forcing alone (8) and that wind variability may also be important in forcing overturning variability at 26.5°N on decadal time scales (9). These studies, along with other modeling results suggesting that buoyancy-forced MOC changes have larger amplitude in the subpolar North Atlantic (SPNA; 10), led to strong interest in a complementary measure of the overturning circulation in this region, where the link between deep water mass formation and overturning variability could be directly assessed. Underscoring the importance of this assessment, the most recent Intergovernmental Panel on Climate Change report projects a MOC slowdown in the 21st century and attributes that slowdown to a reduction in deep convection in the North Atlantic (11). Furthermore, evidence continues to mount that sustained observations of the MOC are needed to understand the potential impact of overturning variability on anthropogenic carbon uptake and storage in the North Atlantic (12).

OSNAP Observing System

With contributions from the U.S., U.K., Germany, the Netherlands, Canada, and China, the OSNAP observing system (**Fig. 1; 13**) comprises an integrated coast-to-coast array of two sections: OSNAP West, extending from the southeastern Labrador shelf to the southwestern tip of Greenland, and OSNAP East, extending from the southeastern tip of Greenland to the Scottish shelf. Densely spaced OSNAP mooring arrays, which directly measure the temperature, salinity

and velocity fields, are in place at continental boundaries and on both flanks of the Reykjanes Ridge; additional dynamic height moorings at key locations allow us to estimate geostrophic flows (**Fig. 2**). Glider surveys along topographically complex sections of OSNAP East complement the moored arrays. The observing system also includes subsurface acoustically-tracked floats in order to trace the pathways of overflow waters in the basin. We report here the MOC, MHT (meridional heat transport) and MFT (meridional freshwater transport) time series from the full installation of the arrays in August 2014 until the first complete data recovery in April 2016. In addition to the OSNAP data, our MOC, MHT and MFT estimates rely on Argo profiling float data, satellite altimetry, and surface wind fields (*14*).

The deployment of the OSNAP array in the summer of 2014 was auspiciously timed: the following two winters produced strong cooling in the western SPNA, with clear signatures of newly-formed water in the Irminger Sea (*15-17*) and mixed-layer depths in the range of 1500–2000 m in the Labrador Sea (*16, 18*). Convection to these depths has not occurred since the mid-1990s when record deep water mass formation took place. Large pools of low salinity waters in these basins (**Fig. 2**) are a strong signature of the recent convection.

MOC definition

We define the MOC as the maximum of the overturning streamfunction (in Sv, where $1 \text{ Sv} = 10^6 \text{ m}^3 \text{ s}^{-1}$) in density space (see Supplementary Materials). We choose density coordinates for our calculation because we are interested in the total volume of buoyant water moving northward (the upper limb) that is balanced by denser, deeper waters moving southward (the lower limb) across the OSNAP section. Here the MOC upper (lower) limb is defined as the transport between

the sea surface (bottom) and the density surface at which the overturning streamfunction reaches a maximum. Essentially, the MOC in density space measures the transformation of less dense waters to more dense waters that occurs poleward of the OSNAP line. We note that this choice is particularly apt for the subpolar basin where strongly sloped isopycnals (**Fig. 2**) confound the interpretation of the MOC calculated in depth space (19, 20). By way of illustration, an integration of the flow across ~500 m would include the warm, relatively buoyant northward-flowing waters in the eastern part of the basin and the cold, relatively dense southward flowing waters off the east coast of Greenland, leading to an underestimate of the amount of water transformed, or “overturned”, from one density class to another (Table S2).

We refer to our MOC measure as the ‘overturning’ and make no assumptions about its driving mechanisms, i.e. the overturning can be impacted by buoyancy and/or wind forcing. We use Monte Carlo simulations to estimate the mean MOC, as well as the mean MHT and MFT, and to provide an estimate of the uncertainty in those means (see Supplementary Materials). All reported deviations (\pm) from the mean are uncertainty estimates, unless indicated otherwise. Finally, we note that the MOC definition reduces the complexity of the circulation across the OSNAP line to a 2-layer system, a simplification that is robust for OSNAP East, yet less so for OSNAP West due to a number of opposing flows in that basin (Fig. S1B).

Elements of the overturning and gyre circulation in the subpolar North Atlantic

A view of salinity and the west-to-east cumulative volume transport for the upper and lower limbs across the OSNAP line reveals the key elements of both the overturning and gyre circulation in the subpolar North Atlantic (**Fig. 2**). Across the Labrador Basin, the large pool of

low salinity water that reaches from the surface to ~ 1500 m marks the Labrador Sea Water (LSW), the shallowest component of the MOC lower limb. Some of this water mass is exported to the subtropics, while some recirculates within the subpolar basin, as revealed by the pool of relatively fresh water at intermediate depths (1000 to 2000 m) in the Iceland basin. A mixture of LSW and locally formed intermediate water is also visible in the Irminger Sea (500 to 1500 m). The western and eastern boundary currents in the Labrador Basin have strong transports, particularly so for the lower limb where transports reach ~ 30 Sv. However, the relatively small cumulative transport across the Labrador Sea in both the upper and lower limbs reveals that these opposing boundary currents are largely carrying waters of the same density, i.e., there is little density transformation or overturning across this basin over this time period.

Across OSNAP East, strong boundary currents with broader opposing flows in the basin interior are also evident in the lower limb (**Fig. 2**). Here, however, there is an appreciable accumulation of southward flow (~ 12 Sv), helped in part by the entry of cold Nordic Seas overflow waters into the subpolar basin. The relatively salty Iceland Scotland Overflow Water flows southward along the eastern flank of the Reykjanes Ridge and the fresher Denmark Strait Overflow Water flows southward in the deep boundary current off East Greenland. The net southward transport of these deep components of the lower limb is largely balanced by the northward-flowing North Atlantic Current, which carries warm, salty waters across the easternmost part of the OSNAP section, forming the bulk of the upper MOC limb.

OSNAP MOC time series

Over the 21-month observational period, the MOC across the entire OSNAP section shows striking temporal variability (**Fig. 3**), with 30-day means from 8.1 to 24.1 Sv, a range comparable to that observed at the RAPID-MOCHA array (21) and the OVIDE section (22). Not surprisingly, the daily means show a larger range, likely a result of high-frequency wind variability over the basin. Though we note a MOC peak in the summer of 2015, no evidence of seasonality can be gleaned from this short record. The net southward Ekman transport (-1.72 ± 0.02 Sv), due to the predominantly westerly winds across the OSNAP line, contributes only minimally to the time-mean and time-varying MOC (**Fig. 3**).

These time series highlight the most striking aspect of this 21-month record, namely the dominance of the overturning circulation across OSNAP East (15.6 ± 0.8 Sv) over that across OSNAP West (2.1 ± 0.3 Sv), the former ~ 7 times greater than the latter. Note that the sum of the MOC estimates across these two sections exceeds the MOC across the entire section (14.9 ± 0.9 Sv) because of cancellations between northward and southward transports. Specifically, southward currents along the east Greenland coast that round Cape Farewell act to cancel some of the northward flow in the same density class along the west Greenland coast, thus making the MOC estimate across the entire section less than the sum of its parts. Note that the OSNAP East MOC estimate and the MOC estimate across the entire section are not distinguishable given our measure of uncertainty.

The overturning circulation across OSNAP East also dominates in terms of temporal variability. Overturning variability across this section explains 88% of the variance in the MOC across the entire section, far exceeding the contribution of OSNAP West (25%). The MOC time series

across the two separate sections are only weakly correlated (at zero lag $r=0.25$; the correlation is strongest ($r=-0.34$) when MOC at OSNAP East leads by 4 months). A longer time series will considerably aid our understanding of the relationship between these two time series.

5 The contrast between the small overturning measure for OSNAP West and the signature of strong local convection (i.e., the homogenous water mass) in this basin is sharp, but not altogether surprising. A number of studies over the past decade have suggested that boundary current strength, exchange between the boundary and the basin interior, and/or other physics allow for a disconnect between local water mass production and its export out of the basin (23-10 25). These early OSNAP results provide support for that disconnect.

Comparison with other MOC estimates

A comparison of basin-wide MOC estimates in the North Atlantic is now possible with the OSNAP and RAPID-MOCHA arrays (Table S3). Over a comparable time period, the OSNAP MOC mean is weaker by ~ 2 Sv than the MOC at 26.5°N (16.8 Sv for 2014-2016; 21). While this RAPID-MOCHA MOC estimate is calculated in depth space, a measure in density space has been shown to be nearly identical due to the relatively flat isopycnals across the subtropical gyre (19). A difference of 2 Sv is not large in light of the ~ 1 Sv uncertainty in the estimates of both the OSNAP (see above) and RAPID-MOCHA means (26). Insight into whether the subpolar MOC is actually weaker than the 15 20 subtropical MOC will likely have to wait until a longer OSNAP time series is secured. Finally, the OSNAP estimate falls near the mid-point of the large range of SPNA MOC estimates predicted by a suite of global ocean-sea-ice models (~ 5 -25 Sv; 27). The OSNAP observations will help narrow the range of these model estimates by providing useful benchmarks and validations.

Comparisons of the MOC across OSNAP East and West with the MOC from geographically similar locations are generally favorable. The OSNAP West estimate is consistent with the mean derived using Argo floats in the vicinity of the AR7W line from 2002-2016 (2.5 Sv; 28) and with the mean estimated from summer hydrography and PALACE floats (2 Sv; 25) in the same region between 1990-1997. There are two MOC estimates at 59.5°N, just north of the OSNAP East line: one is a 2002-2008 mean summer estimate (16.6 ± 1.1 Sv; 29) based on altimetry and hydrography, and the other is a long-term mean estimate between early 2012 to early 2016 based on hydrography and shipboard ADCP (18.4 ± 3.4 Sv; 30). Given the uncertainties in all estimates, the OSNAP East MOC is largely consistent with these measures despite the fact that the records are non-contemporaneous. Finally, the OSNAP East estimate is somewhat lower than the MOC estimate reconstructed from altimetry and Argo along the OVIDE line (which runs from Greenland to Portugal; **Fig. 1**) between 1993-2010 (18.1 ± 1.4 Sv; 22). This difference is perhaps attributable to the presence of a subtropical component in the total OVIDE overturning, though further analysis is needed to confirm this supposition.

Meridional Heat and Freshwater Transports

An estimate of MHT across the entire OSNAP section yields a mean and uncertainty of 0.45 ± 0.02 PW. The record is marked by strong temporal variability (**Fig. 4**), with a range of 0.33 to 0.59 PW. This variability is largely determined by the variable flow field, rather than by temperature fluctuations: velocity variance explains 93% of the MHT variance. To understand the circulation features responsible for this heat transport, we decompose the total transport into an overturning component and an ‘isopycnal transport’ component (see Supplementary Materials). In other words, we

partition the heat transport into that accomplished by warm water moving northward in the upper limb and cold water moving southward in the lower limb (the overturning component) and that accomplished by opposing northward and southward flows (carrying waters with different temperatures) on the same isopycnal (the isopycnal transport component). This decomposition reveals that the overturning component dominates the total MHT (**Fig. 4**), accounting for 73% of the mean and 87% of the variance. Given this dominance, it is not surprising that the heat transport across OSNAP East (0.38 ± 0.02 PW) greatly exceeds that of OSNAP West (0.080 ± 0.004 PW) (Table S3). Finally, we note that a decomposition of heat transport in depth space (Fig. S2) yields a relatively minor contribution of the overturning component to the total, illustrating the suitability of density coordinates for an estimate of how water mass transformation impacts heat transport in the subpolar region.

The mean MFT across the entire OSNAP section is estimated at -0.33 ± 0.01 Sv. This record also reveals strong temporal variability (**Fig. 4**), with a range of -0.45 to -0.21 Sv. As with MHT, the majority of the MFT variance is explained by the variable flow field: velocity variability (rather than salinity variability) explains 78% of the total MFT variance. From the decomposition, we find that, on average, overturning accounts for 62% of the total freshwater transport across the full OSNAP array. However, there is considerable range in that partitioning. In fact, there is a period of time (July to November of 2015) when the isopycnal component is larger. During this time period, the net southward flux of freshwater due to opposing flows on isopycnals is larger than the net southward freshwater flux accomplished by the overturning. Also of note is that the contribution from OSNAP West (-0.184 ± 0.004 Sv) to the total MFT actually exceeds that for OSNAP East (-0.14 ± 0.01 Sv) (Table 3), in contrast to their relative contributions to MHT. Finally, we note that we currently use monthly mean model velocities and monthly climatological means for salinity and temperature across

the Labrador Current inshore of 300 m (see Supplementary Materials), where moored instrumentation is subject to disruption due to heavy fishing activity in the region. An exploration of alternative means for estimating the inshore velocity and properties is underway.

5 In summary, heat transport across the entire OSNAP section is principally accomplished by the overturning, which is largely focused across OSNAP East. In contrast, freshwater transport across OSNAP West is larger than that across OSNAP East, and the isopycnal component can at times exceed the overturning component. These differences can be understood in the context of circulation differences across OSNAP East and West (Fig. 2). The upper limb of OSNAP East has an isopycnal
10 circulation (the volume of water with opposing northward and southward flows) of ~ 13 Sv, which nearly matches the transport of the overturning circulation (~ 15 Sv). However, the upper limb of OSNAP West has a much stronger isopycnal circulation (~ 11 Sv) than overturning circulation (~ 2 Sv). Thus, it appears that salinity gradients on isopycnals across OSNAP West may be driving a sizeable portion of the freshwater flux, a supposition that will be explored in future work by partitioning the
15 MHT and MFT components across OSNAP East and West separately. Such partitioning may reconcile the results here with an earlier study (25) which found that isopycnal transport, rather than overturning, was the largest contributor to heat flux across the Labrador Sea during the 1990s.

Comparison with the RAPID-MOCHA MHT and MFT estimates

20 The simultaneous measure of MHT and MFT across the transatlantic OSNAP and RAPID-MOCHA lines provides for the first time an *in situ* measure of the heat and freshwater flux divergence between the two latitudes, quantities relevant to our understanding of climate variability and to MOC stability. The heat transport divergence between these two lines, 0.80

PW (Table S3), is the amount of heat stored or lost to the atmosphere as the warm Gulf Stream and North Atlantic Current waters move northward from RAPID-MOCHA to OSNAP.

Likewise, the southward OSNAP MFT is 0.10 Sv weaker than that reported at RAPID-MOCHA, suggesting a net freshwater storage or addition to the Atlantic between the two latitudes. These
5 divergences provide an important validation for atmospheric reanalyses and air-sea flux estimates, which currently underestimate the northward ocean heat transport at the OSNAP latitudes (31).

Implications

10 These OSNAP results show that the conversion of warm, salty, shallow Atlantic waters into cold, fresh, deep waters accomplished north of the OSNAP East line is largely responsible for overturning and its variability in the subpolar basin over this observational record. Despite signatures of substantial water mass formation, the Labrador Sea contributes minimally to the total overturning. This result is consistent with a number of recent studies that have raised
15 questions about the importance of LSW formation to MOC variability. An examination of transports at 53°N (the westernmost array in the OSNAP West line) shows no clear link between boundary current export and LSW formation in the basin interior (32); a modeling study (33) finds no relationship between the volume of LSW formed in the Labrador Sea and its export to the subtropical gyre; and even further downstream at the RAPID-MOCHA array, LSW
20 variability is relatively weak over the record and plays little role in the recent overturning decline (21).

Past modeling studies, however, have shown that density anomalies in the Labrador Sea are strongly associated with downstream MOC variability on multiannual to decadal time scales (e.g., 34-37). Even though these time scales exceed the OSNAP observational record to date, the OSNAP MOC estimate stands in stark contrast to a picture of the MOC dominated by Labrador Sea convection. Furthermore, recent studies have used densities at mid-depth in the Labrador Sea, assumed to be linked to convection in that basin, as proxies for the modern and paleo Atlantic MOC (38-40). A reconciliation with these past modeling results is possible if the density anomalies in the Labrador Sea are signatures of upstream density anomalies imported from the eastern subpolar gyre and/or have a remote impact on the overturning between Greenland and Scotland. With either scenario, Labrador Sea density remains a signature of the MOC across the subpolar basin, yet not of local convection. Further modeling studies in light of these new observations is warranted, as is continued work on the use and interpretation of proxies (41).

While these OSNAP observations invite a reexamination of some long-held assumptions about the MOC in the subpolar North Atlantic, a longer time series will be needed to determine whether the strong MOC across OSNAP East is consistent with buoyancy forcing north of the line, and whether the relatively small overturning across OSNAP West reported here is representative of its contribution on longer time scales. Finally, we note that while the MOC and MHT to date are dominated by OSNAP East dynamics, OSNAP West dynamics play a large role in the total MFT.

Next Steps

An extension of this record is necessary in order to determine seasonal and interannual variability and to detect any long-term trends. However, it is of sufficient length to provide an important baseline for numerical models, essential to placing the observations in a broader spatial and temporal context.

Another important next step for the ocean community is to place these OSNAP results in the context of other Atlantic MOC measures to understand how overturning impacts the basin-wide transport and storage of heat, freshwater and carbon. A continuation of measurements is needed for this tall order, but the observing systems put in place over the past fifteen years by the international ocean community, already yielding rich dividends, are leading us in that direction.

References and Notes:

1. W. S. Broecker, *The Glacial World According to Wally*. (Eldigio Press, Lamont-Doherty earth observatory of Columbia University, Palisades, New York, ed. 2, 1995), vol. 318.
2. National Research Council, *Abrupt Climate Change: Inevitable Surprises*. (National Academies Press, Washington, DC, 2002), pp. 244.
3. S. A. Cunningham *et al.*, Temporal variability of the Atlantic meridional overturning circulation at 26.5°N. *Science* **317**, 935-938 (2007).
4. M. Srokosz, H. Bryden, Observing the Atlantic meridional overturning circulation yields a decade of inevitable surprises. *Science* **348**, 1255575 (2015).
5. R. J. Bingham, C. W. Hughes, V. Roussenov, R. G. Williams, Meridional coherence of the North Atlantic meridional overturning circulation. *Geophys. Res. Lett.* **34**, L23606 (2007).
6. M. S. Lozier, V. Roussenov, M. S. C. Reed, R. G. Williams, Opposing decadal changes for the North Atlantic meridional overturning circulation. *Nature Geosci.* **3**, 728-734 (2010).

7. R. G. Williams, V. Roussenov, D. Smith, M. S. Lozier, Decadal evolution of ocean thermal anomalies in the North Atlantic: The effects of Ekman, overturning, and horizontal transport. *J. Climate* **27**, 698-719 (2014).
8. J. Zhao, W. Johns, Wind-forced interannual variability of the Atlantic meridional overturning circulation at 26.5°N. *J. Geophys. Res. Oceans* **119**, 2403-2419 (2014).
9. I. Polo, J. Robson, R. Sutton, M. A. Balmaseda, The importance of wind and buoyancy forcing for the boundary density variations and the geostrophic component of the AMOC at 26°N. *J. Phys. Oceanogr.* **44**, 2387-2408 (2014).
10. A. Biastoch, C. W. Böning, J. Getzlaff, J.-M. Molines, G. Madec, Causes of interannual–decadal variability in the meridional overturning circulation of the midlatitude North Atlantic Ocean. *J. Climate* **21**, 6599-6615 (2008).
11. IPCC, *Climate Change 2013: The Physical Science Basis*. T.F. Stocker, D. Qin, G.-K. Plattner, M. Tignor, S.K. Allen, J. Boschung, A. Nauels, Y. Xia, V. Bex and P.M. Midgley, Eds., (Cambridge University Press, Cambridge, United Kingdom and New York, NY, USA, 2013).
12. G. A. McKinley, A. R. Fay, N. S. Lovenduski, D. J. Pilcher, Natural variability and anthropogenic trends in the ocean carbon sink. *Annu. Rev. Mar. Sci.* **9**, 125-150 (2017).
13. M. S. Lozier *et al.*, Overturning in the Subpolar North Atlantic Program: A new international ocean observing system. *Bull. Amer. Meteor. Soc.* **98**, 737-752 (2017).
14. F. Li, M. S. Lozier, W. E. Johns, Calculating the meridional volume, heat, and freshwater transports from an observing system in the subpolar North Atlantic: Observing system simulation experiment. *J. Atmos. Oceanic Technol.* **34**, 1483-1500 (2017).

15. M. F. de Jong, L. de Steur, Strong winter cooling over the Irminger Sea in winter 2014–2015, exceptional deep convection, and the emergence of anomalously low SST. *Geophys. Res. Lett.* **43**, 7106-7113 (2016).
16. A. Piron, V. Thierry, H. Mercier, G. Caniaux, Gyre-scale deep convection in the subpolar North Atlantic Ocean during winter 2014-2015. *Geophys. Res. Lett.* **44**, 1439-1447 (2017).
17. F. Fröb *et al.*, Irminger Sea deep convection injects oxygen and anthropogenic carbon to the ocean interior. *Nat. Commun.* **7**, (2016).
18. I. Yashayaev, J. W. Loder, Further intensification of deep convection in the Labrador Sea in 2016. *Geophys. Res. Lett.* **44**, 1429-1438 (2017).
19. X. Xu, E. P. Chassignet, W. E. Johns, J. S. William, E. J. Metzger, Intraseasonal to interannual variability of the Atlantic meridional overturning circulation from eddy-resolving simulations and observations. *J. Geophys. Res. Oceans* **119**, 5140-5159 (2014).
20. N. P. Holliday *et al.*, Subpolar North Atlantic overturning and gyre-scale circulation in the summers of 2014 and 2016. *J. Geophys. Res. Oceans* **123**, 4538-4559 (2018).
21. D. A. Smeed *et al.*, The North Atlantic Ocean is in a state of reduced overturning. *Geophys. Res. Lett.* **45**, 1527-1533 (2018).
22. H. Mercier *et al.*, Variability of the meridional overturning circulation at the Greenland-Portugal OVIDE section from 1993 to 2010. *Prog. Oceanogr.* **132**, 250-261 (2015).
23. M. A. Spall, Boundary currents and watermass transformation in marginal seas. *J. Phys. Oceanogr.* **34**, 1197-1213 (2004).
24. F. Straneo, On the connection between dense water formation, overturning, and poleward heat transport in a convective basin*. *J. Phys. Oceanogr.* **36**, 1822-1840 (2006).

25. R. S. Pickart, M. A. Spall, Impact of Labrador Sea convection on the North Atlantic meridional overturning circulation. *J. Phys. Oceanogr.* **37**, 2207-2227 (2007).
26. G. D. McCarthy *et al.*, Measuring the Atlantic meridional overturning circulation at 26°N. *Prog. Oceanogr.* **130**, 91-111 (2015).
- 5 27. G. Danabasoglu *et al.*, North Atlantic simulations in coordinated ocean-ice reference experiments phase II (CORE-II). Part I: mean states. *Ocean Model.* **73**, 76-107 (2014).
28. J. Holte, F. Straneo, Seasonal overturning of the Labrador Sea as observed by Argo floats. *J. Phys. Oceanogr.* **47**, 2531-2543 (2017).
29. A. Sarafanov *et al.*, Mean full-depth summer circulation and transports at the northern periphery of the Atlantic Ocean in the 2000s. *J. Geophys. Res. Oceans* **117**, (2012).
- 10 30. T. Rossby, G. Reverdin, L. Chafik, H. Søliland, A direct estimate of poleward volume, heat, and freshwater fluxes at 59.5°N between Greenland and Scotland. *J. Geophys. Res. Oceans* **122**, 5870-5887 (2017).
31. K. E. Trenberth, J. M. Caron, Estimates of meridional atmosphere and ocean heat transports. *J. Climate* **14**, 3433-3443 (2001).
- 15 32. R. Zantopp, J. Fischer, M. Visbeck, J. Karstensen, From interannual to decadal: 17 years of boundary current transports at the exit of the Labrador Sea. *J. Geophys. Res. Oceans* **122**, 1724-1748 (2017).
33. S. Zou, M. S. Lozier, Breaking the linkage between Labrador Sea Water production and its advective export to the subtropical gyre. *J. Phys. Oceanogr.* **46**, 2169-2182 (2016).
- 20 34. C. Eden, J. Willebrand, Mechanism of interannual to decadal variability of the North Atlantic circulation. *J. Climate* **14**, 2266-2280 (2001).

35. D. A. Bailey, P. B. Rhines, S. Häkkinen, Formation and pathways of North Atlantic Deep Water in a coupled ice–ocean model of the Arctic–North Atlantic Oceans. *Climate Dyn.* **25**, 497-516 (2005).
36. J. Getzlaff, C. W. Böning, C. Eden, A. Biastoch, Signal propagation related to the North Atlantic overturning. *Geophys. Res. Lett.* **32**, (2005).
37. G. Danabasoglu *et al.*, Variability of the Atlantic meridional overturning circulation in CCSM4. *J. Climate* **25**, 5153-5172 (2012).
38. J. Robson, P. Ortega, R. Sutton, A reversal of climatic trends in the North Atlantic since 2005. *Nature Geosci.* **9**, 513-517 (2016).
39. L. C. Jackson, K. A. Peterson, C. D. Roberts, R. A. Wood, Recent slowing of Atlantic overturning circulation as a recovery from earlier strengthening. *Nature Geosci.* **9**, 518-522 (2016).
40. D. J. R. Thornalley *et al.*, Anomalously weak Labrador Sea convection and Atlantic overturning during the past 150 years. *Nature* **556**, 227-230 (2018).
41. F. Li, M. S. Lozier, On the linkage between Labrador Sea Water volume and overturning circulation in the Labrador Sea: A case study on proxies. *J. Climate* **31**, 5225-5241 (2018).
42. M. Bersch, I. Yashayaev, K. P. Koltermann, Recent changes of the thermohaline circulation in the subpolar North Atlantic. *Ocean Dyn.* **57**, 223-235 (2007).
43. K. Våge *et al.*, The Irminger Gyre: Circulation, convection, and interannual variability. *Deep-Sea Res. I* **58**, 590-614 (2011).
44. N. P. Holliday *et al.*, Multidecadal variability of potential temperature, salinity, and transport in the eastern subpolar North Atlantic. *J. Geophys. Res. Oceans* **120**, 5945-5967 (2015).

45. I. Yashayaev, J. W. Loder, Recurrent replenishment of Labrador Sea Water and associated decadal-scale variability. *J. Geophys. Res. Oceans* **121**, 8095-8114 (2016).
46. R. A. Locarnini *et al.*, "World Ocean Atlas 2013, Volume 1: Temperature," (NOAA Atlas NESDIS 73, 2013).
- 5 47. M. M. Zweng *et al.*, "World Ocean Atlas 2013, Volume 2: Salinity," (NOAA Atlas NESDIS 74, 2013).
48. D. P. Dee *et al.*, The ERA-Interim reanalysis: configuration and performance of the data assimilation system. *Quart. J. Roy. Meteor. Soc.* **137**, 553-597 (2011).
49. C. Gourcuff, P. Lherminier, H. Mercier, P. Y. Le Traon, Altimetry combined with
10 hydrography for ocean transport estimation. *J. Atmos. Oceanic Technol.* **28**, 1324-1337 (2011).
50. T. J. Sherwin, D. Aleynik, E. Dumont, M. E. Inall, Deep drivers of mesoscale circulation in the central Rockall Trough. *Ocean Sci.* **11**, 343-359 (2015).
51. C. W. Böning, M. Scheinert, J. Dengg, A. Biastoch, A. Funk, Decadal variability of subpolar gyre transport and its reverberation in the North Atlantic overturning. *Geophys. Res. Lett.* **33**, L21S01 (2006).
- 15 52. G. Han, Z. Ma, Z. Long, W. Perrie, J. Chassé, Climate change on Newfoundland and Labrador shelves: Results from a regional downscaled ocean and sea-ice model under an A1B forcing scenario 2011–2069. *Atmo.-Ocean*, 1-15 (2018).
- 20 53. B. Curry, C. M. Lee, B. Petrie, R. E. Moritz, R. Kwok, Multiyear volume, liquid freshwater, and sea ice transports through Davis Strait, 2004-10*. *J. Phys. Oceanogr.* **44**, 1244-1266 (2014).

54. R. A. Woodgate, Increases in the Pacific inflow to the Arctic from 1990 to 2015, and insights into seasonal trends and driving mechanisms from year-round Bering Strait mooring data. *Prog. Oceanogr.* **160**, 124-154 (2018).
55. M. M. Hall, H. L. Bryden, Direct estimates and mechanisms of ocean heat-transport. *Deep-Sea Res. I* **29**, 339-359 (1982).
56. W. E. Johns *et al.*, Continuous, Array-based estimates of Atlantic Ocean heat transport at 26.5°N. *J. Climate* **24**, 2429-2449 (2011).
57. R. E. Thomson, W. J. Emery, “Time-series Analysis Methods” in *Data Analysis Methods in Physical Oceanography*, R. E. Thomson, W. J. Emery, Eds. (Elsevier Science, 2014), chap. 5, pp. 432.
58. D. R. Jackett, T. J. McDougall, A neutral density variable for the world’s oceans. *J. Phys. Oceanogr.* **27**, 237-263 (1997).
59. E. L. McDonagh *et al.*, Continuous estimate of Atlantic oceanic freshwater flux at 26.5°N. *J. Climate* **28**, 8888-8906 (2015).

Acknowledgements

We gratefully acknowledge exceptional support provided by the officers, crews and technicians of the R/V Neil Armstrong, R/V Knorr, R/V Pelagia, R/V Maria S Merian, CCGS Hudson, and RRS Discovery in the completion of the fieldwork. We are also grateful to Eric Itsweire for his guidance and support during the initiation of this program. Argo data were collected and made freely available by the International Argo Program and the national programs that contribute to it (<http://www.argo.ucsd.edu>, <http://argo.jcommops.org>). The Argo Program is part of the Global Ocean Observing System (<http://doi.org/10.17882/42182>). The Ssalto/Duacs altimeter products

were produced and distributed by the Copernicus Marine and Environment Monitoring Service (CMEMS) (<http://www.marine.copernicus.eu>). **Funding:** We gratefully acknowledge funding from the Physical Oceanography Program of the U.S. National Science Foundation; UK's Natural Environment Research Council programmes UK OSNAP, the Extended Ellett Line and ACSIS (National Capability). Additional support was received from the European Union 7th Framework Programme (FP7 2007-2013) under grant agreement 308299 (NACLIM) and the Horizon 2020 research and innovation program under grant agreements 727852 (Blue-Action), 308299 (NACLIM), 678760 (ATLAS) and 633211 (AtlantOS). We also acknowledge support from the French Centre National de la Recherche Scientifique, from China's national key research and development projects (2016YFA0601803) and the Fundamental Research Funds for the Central Universities (201424001). Support for the 53°N array by the RACE program of the German Ministry BMBF is gratefully acknowledged, as is the contribution from Fisheries and Oceans Canada's (DFO's) Atlantic Zone Off-shelf Monitoring Program (AZOMP). **Author contributions:** MSL, SB, ASB, SAC, LdS, BdY, JF, BJWG, NPH, MEI, WEJ, HLJ, JK, XL, DPM, RSP, FS, VT, RGW and CW conceptualized and initiated the OSNAP project. MSL, SB, ASB, SAC, LdS, BdY, JF, BJWG, NPH, MEI, WEJ, HLJ, JK, XL, DPM, RSP, FS, RGW, CW and JY acquired the financial support for the projects leading to this publication. MSL managed and coordinated responsibilities for the research activity, planning, and execution. FB, SAC, MFdJ, LdS, SFG, NPH, AH, LH, MEI, WEJ, CJ, JK, GK, IALB, FL, NM, MO, RSP, ALR, DR, DJT, IY and JZ were responsible for data collection, processing and quality control. MFdJ, NPH, LH, WEJ, JK, IALB, RSP and JZ verified transport estimates at individual arrays. ASB, SAC, NPH, LH, WEJ, FL, MSL, HM and CW developed data analysis methodology. FL synthesized the data and carried out data analyses. MSL wrote the initial draft. FL prepared and created

visualization/data presentation. SB, ASB, SAC, MFdJ, LdS, BdY, SFG, NPH, LH, MEI, WEJ, HLJ, CJ, JK, IALB, FL, XL, DPM, HM, MO, RSP, FS, VT, CW and RGW reviewed and edited the manuscript. **Competing interest:** The authors declare that they have no competing interests.

Data and materials availability: All data products from OSNAP including those that support the main findings of this paper are publicly available at www.o-snap.org. The derived data (i.e., MOC, MHT and MFT) are also available in Duke Digital Repository (doi: 10.7924/r4z60gf0f). Calibrated and quality-controlled data from moored instruments and gliders were generated by each participating group and are available in designated repositories with identifiers as follows: Canadian shelf break array, doi:10.5281/zenodo.1285757; US Labrador Sea eastern boundary array, doi: 10.7924/r4fj2dr7k; US east Cape Farewell slope array, doi:10.7924/r4fb50z9b; NOC DWBC array, doi:10/cwf4; NIOZ western Mid-Atlantic-Ridge array, doi:10.4121/uuid:77b2c4fc-c253-4494-91bd-8d1ef66a014a, doi:10.4121/uuid:9ae97ceb-39e4-43ec-abdb-614103285c16; US eastern Mid-Atlantic-Ridge array, doi:10.7924/r42n52w51; WHOI/OUC gliders, doi:10.7924/r4m905g03; SAMS gliders, doi:10/ckbr; SAMS Rockall Trough array, doi:10/cwf3.

Supplementary Materials:

Materials and Methods

Fig S1 – S2

Table S1 – S3

References (46-59)

Fig. 1. OSNAP observing system. The OSNAP section (red line) superposed on a map of mean absolute dynamic height (m), with bathymetry < 500 m shaded gray. The OSNAP observing system was designed to take advantage of the German Labrador Sea exit array at 53°N (operational since 1997; 32); the recently installed US Global OOI (Ocean Observatories Initiative) node in the southwest Irminger Sea; repeat A1E/AR7E hydrographic sections across the Irminger and Iceland basins; 42, 43); and the Ellett Line in the eastern basin (operational since 1976; 44). OSNAP complements several monitoring programs in the North Atlantic: the Canadian repeat AR7W program in the Labrador Sea; 18, 45); Cape Farewell-Scotland sections at 59.5°N; 29, 30); the French OVIDE line across the eastern North Atlantic, 22); and the UK-US RAPID-MOCHA array at 26.5°N; 3).

Fig. 2. Transport and salinity across the OSNAP section. (A) Top-to-bottom integrated volume transport ($1 \text{ Sv} = 10^6 \text{ m}^3 \text{ s}^{-1}$) accumulated eastward starting at the western edge of the Labrador Basin (black line), with northward transport defined as positive. The upper (red line) and lower (blue line) MOC limbs are shown separately. Shading indicates one standard deviation from the 21-month mean. (B) The OSNAP section with moorings marked by black lines. Vertical magenta lines over the western flank of the Reykjanes Ridge indicate three French moorings, part of the RREX program. Hatching in the eastern Iceland Basin indicates the glider survey domain. Mean salinity (colored, with scale at the right hand side) and potential density (contoured) are calculated from Argo and OSNAP data from August 2014 to April 2016. The solid black line denotes the potential density surface (27.66 kg m^{-3}) that separates the MOC upper and lower limbs (see Fig. S1A).

Fig. 3. MOC and Ekman Transport across the OSNAP section. Black, yellow and blue lines represent the 30-day mean estimates from the full section, OSNAP West and OSNAP East, respectively,

for MOC (solid lines) and Ekman transport (dashed lines). Shading indicates uncertainty in the 30-day means. Uncertainty in the Ekman transports is too small for display (see Table S3). Thin gray lines show the 10-day low-pass filtered daily means for the full OSNAP section. See Supplementary Materials for details on the mean and uncertainty estimates.

5 **Fig. 4. MHT and MFT across the OSNAP section.** (A) Total MHT. (B) Total MFT relative to the 21-month section mean salinity of 34.92 across the full OSNAP section over the period of August 2014 to April 2016 (black lines). Both transports are decomposed into overturning (blue lines) and isopycnal (red lines) components. Shading indicates uncertainty in the 30-day mean estimates. See Supplementary Materials for details on the mean and uncertainty estimates, and

10 the decomposition.

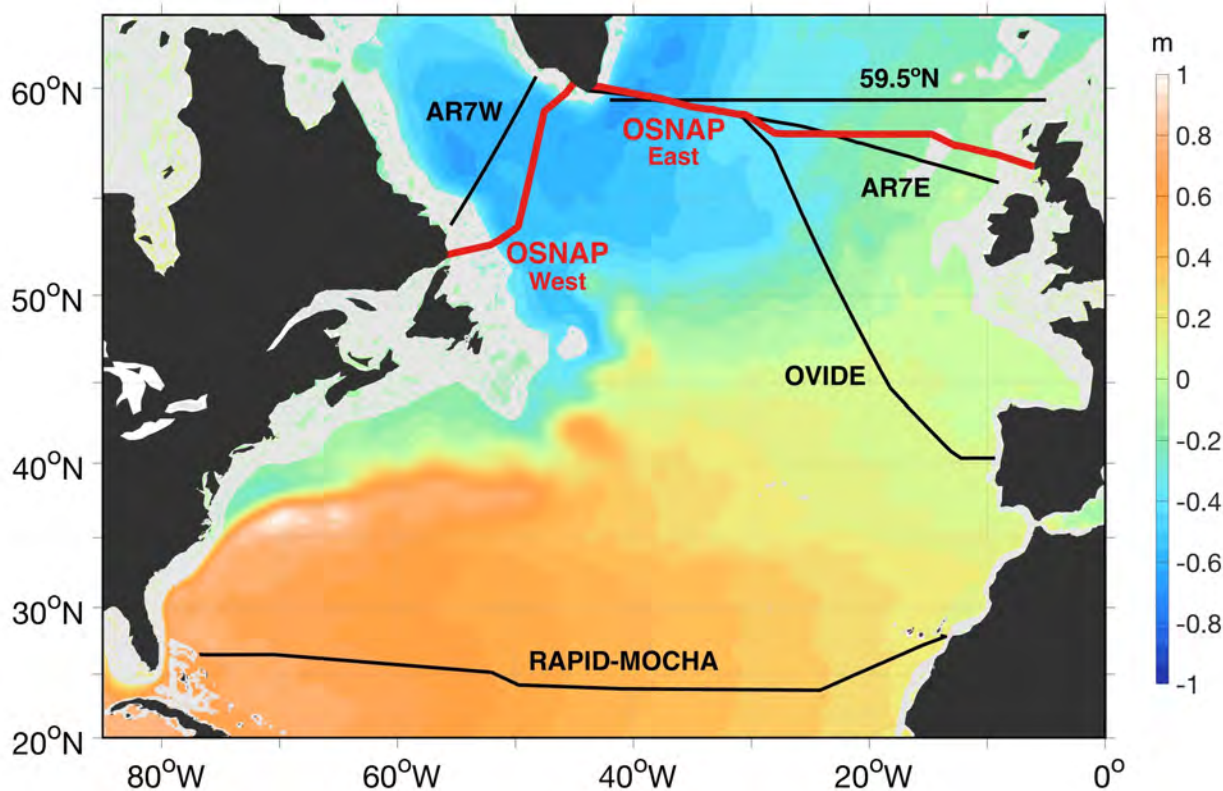


Fig. 1. OSNAP observing system. The OSNAP section (red line) superposed on a map of mean absolute dynamic height (m), with bathymetry < 500 m shaded gray. The OSNAP observing system was designed to take advantage of the German Labrador Sea exit array at 53°N (operational since 1997; 32); the recently installed US Global OOI (Ocean Observatories Initiative) node in the southwest Irminger Sea; repeat A1E/AR7E hydrographic sections across the Irminger and Iceland basins; 42, 43); and the Ellett Line in the eastern basin (operational since 1976; 44). OSNAP complements several monitoring programs in the North Atlantic: the Canadian repeat AR7W program in the Labrador Sea; 18, 45); Cape Farewell-Scotland sections at 59.5°N; 29, 30); the French OVIDE line across the eastern North Atlantic, 22); and the UK-US RAPID-MOCHA array at 26.5°N; 3).

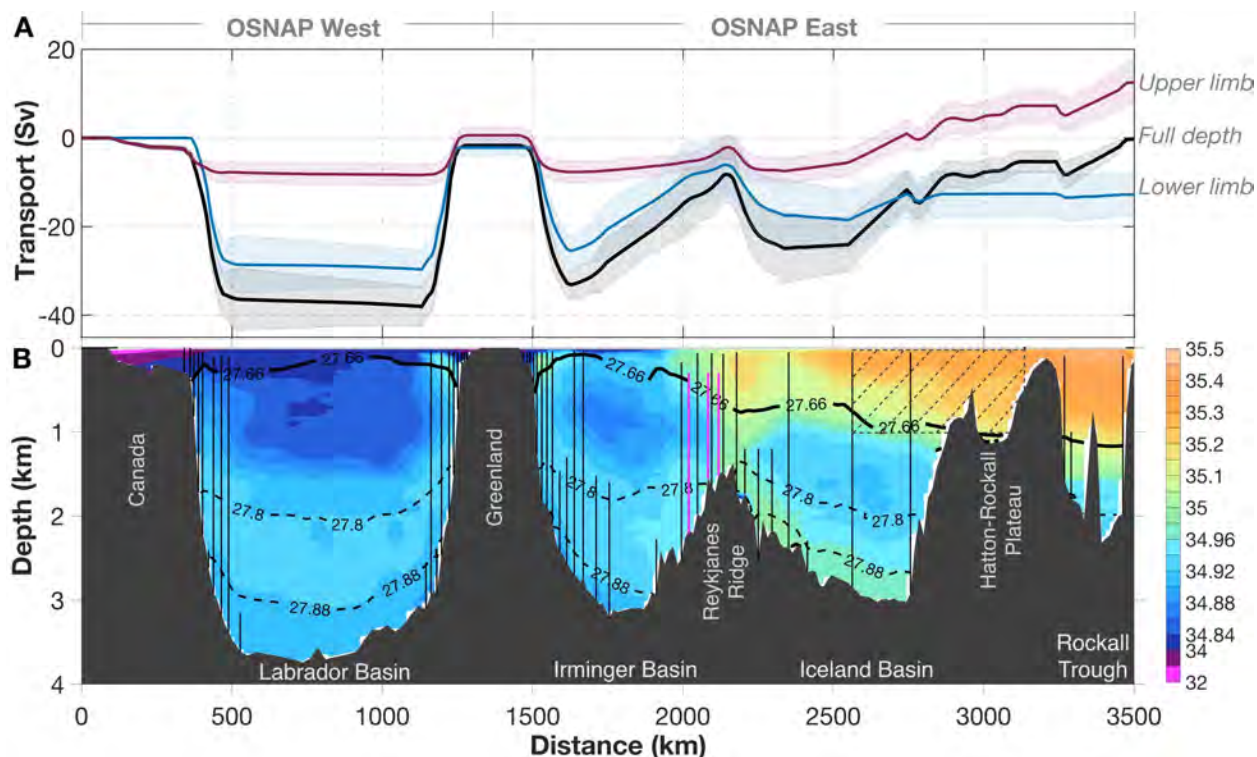


Fig. 2. Transport and salinity across the OSNAP section. (A) Top-to-bottom integrated volume transport ($1 \text{ Sv} = 10^6 \text{ m}^3 \text{ s}^{-1}$) accumulated eastward starting at the western edge of the Labrador Basin (black line), with northward transport defined as positive. The upper (red line) and lower (blue line) MOC limbs are shown separately. Shading indicates one standard deviation from the 21-month mean. (B) The OSNAP section with moorings marked by black lines. Vertical magenta lines over the western flank of the Reykjanes Ridge indicate three French moorings, part of the RREX program. Hatching in the eastern Iceland Basin indicates the glider survey domain. Mean salinity (colored, with scale at the right hand side) and potential density (contoured) are calculated from Argo and OSNAP data from August 2014 to April 2016. The solid black line denotes the potential density surface (27.66 kg m^{-3}) that separates the MOC upper and lower limbs (see Fig. S1A).

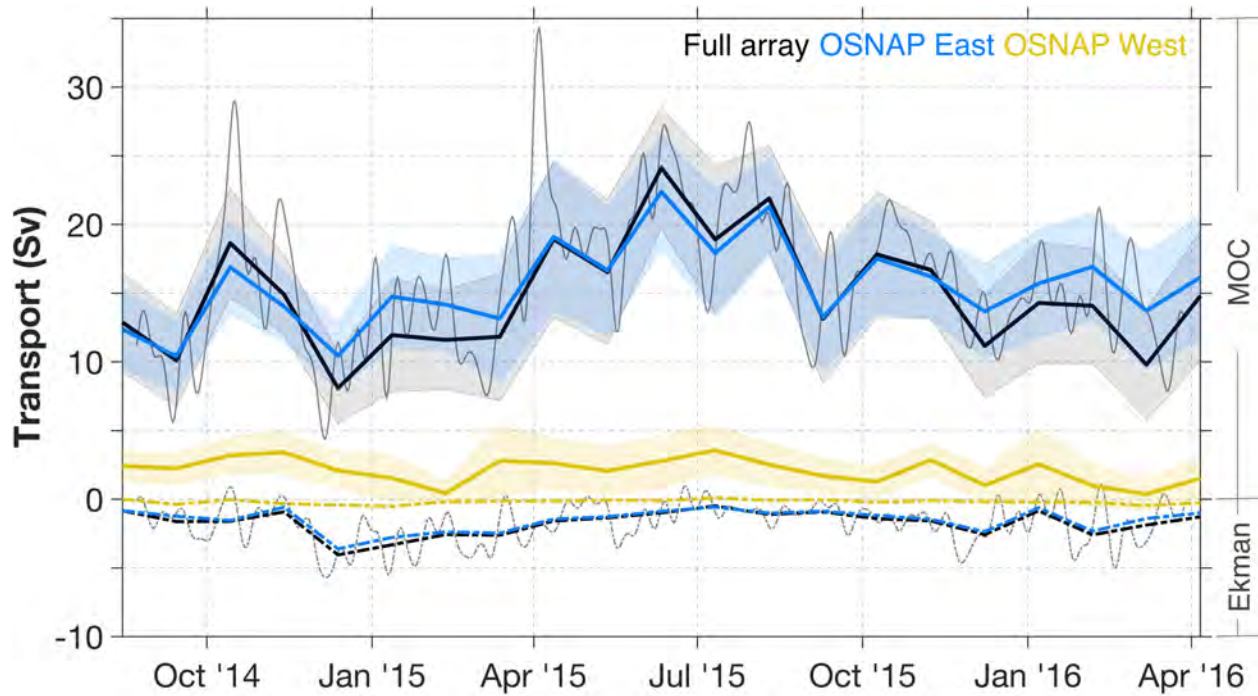


Fig. 3. MOC and Ekman Transport across the OSNAP section. Black, yellow and blue lines represent the 30-day mean estimates from the full section, OSNAP West and OSNAP East, respectively, for MOC (solid lines) and Ekman transport (dashed lines). Shading indicates uncertainty in the 30-day means. Uncertainty in the Ekman transports is too small for display (see Table S3). Thin gray lines show the 10-day low-pass filtered daily means for the full OSNAP section. See Supplementary Materials for details on the mean and uncertainty estimates.

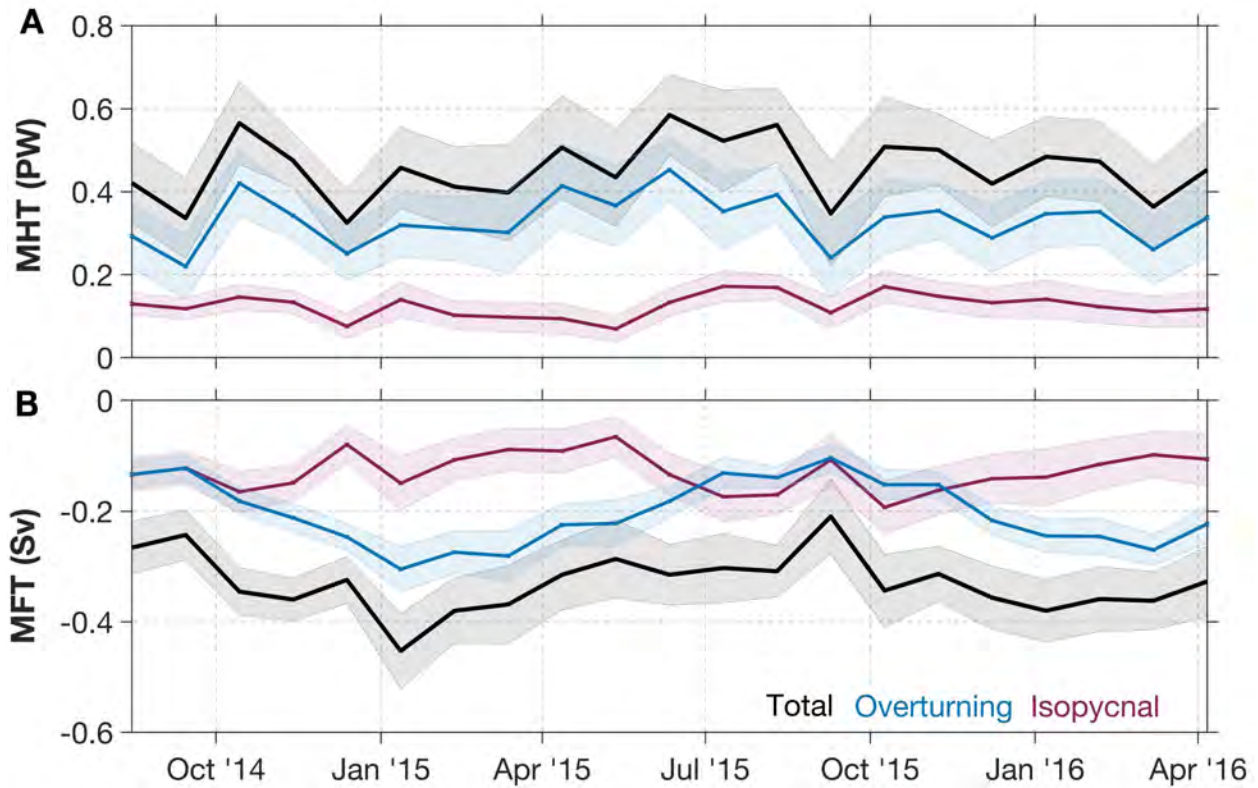


Fig. 4. MHT and MFT across the OSNAP section. (A) Total MHT. **(B)** Total MFT relative to the 21-month section mean salinity of 34.92 across the full OSNAP section over the period of August 2014 to April 2016 (black lines). Both transports are decomposed into overturning (blue lines) and isopycnal (red lines) components. Shading indicates uncertainty in the 30-day mean estimates. See Supplementary Materials for details on the mean and uncertainty estimates, and the decomposition.



Supplementary Materials for

A sea change in our view of overturning– first results from the Overturning in the Subpolar North Atlantic Program

M.S. Lozier*, F. Li*, S. Bacon, F. Bahr, A.S. Bower, S.A. Cunningham, M.F. de Jong, L. de Steur, B. deYoung, J. Fischer, S.F. Gary, B.J.W. Greenan, N.P. Holliday, A. Houk, L. Houpert, M.E. Inall, W.E. Johns, H.L. Johnson, C. Johnson, J. Karstensen, G. Koman, I.A. Le Bras, X. Lin, N. Mackay, D.P. Marshall, H. Mercier, M. Oltmanns, R.S. Pickart, A.L. Ramsey, D. Rayner, F. Straneo, V. Thierry, D.J. Torres, R.G. Williams, C. Wilson, J. Yang, I. Yashayaev, J. Zhao

*Correspondence should be addressed to: mslozier@duke.edu (MSL); feili.li@duke.edu (FL)

This PDF file includes:

Materials and Methods

Figs. S1 to S2

Tables S1 to S3

References (46 – 59)

Materials and Methods

1. MOC, MHT and MFT calculations

Details of all calculation methods and of the observing system experiments run to test OSNAP methodology and array design are in Li *et al.* (14). Here we provide a brief summary.

a. MOC, MHT and MFT definitions

MOC is defined as the maximum of the overturning streamfunction in density space $\Psi(\sigma, t)$:

$$\text{MOC}(t) = \max[\Psi(\sigma, t)] = \max \left[\int_{\sigma_{\min}}^{\sigma} \int_{x_w}^{x_e} v(x, \sigma, t) dx d\sigma \right] \text{ (Sv)}, \quad (\text{S1})$$

where v , the velocity field normal to the OSNAP section, is integrated from west (x_w) to east (x_e) and from the top (σ_{\min}) across all density surfaces. We choose to calculate the MOC in density space in order to quantify the transformation of waters from one density class to another. The MOC upper (lower) limb is defined as the transport between the surface (bottom) and the density at which the overturning function reaches a maximum.

MHT is defined as:

$$\text{MHT}(t) = \rho C_p \int_{\sigma_{\min}}^{\sigma_{\max}} \int_{x_w}^{x_e} v(\sigma, t) \theta(\sigma, t) dx d\sigma \text{ [W]}, \quad (\text{S2})$$

where ρ is potential density, C_p is the specific heat of seawater, θ is potential temperature, and the double integral is taken over all σ surfaces and between the western and eastern boundaries.

MFT is defined as:

$$\text{MFT}(t) = - \int_{\sigma_{\min}}^{\sigma_{\max}} \int_{x_w}^{x_e} v(\sigma, t) \frac{S(\sigma, t) - \bar{S}}{\bar{S}} dx d\sigma \text{ [Sv]}, \quad (\text{S3})$$

where \bar{S} is the area-weighted section mean salinity (34.92 for the whole section, 34.85 for OSNAP West and 34.97 for OSNAP East), and the double integral is taken over all σ surfaces and between the western and eastern boundaries. The resultant MFT is an equivalent freshwater transport that can be interpreted as the volume of water at the section-mean salinity needed to balance the salt flux across the section in each 30-day period.

We follow the convention of positive (negative) values indicating northward (southward) volume (MOC), heat (MHT) and freshwater (MFT) transports.

b. Property and velocity fields

Property and velocity fields are calculated on a grid along the OSNAP section. The grid uses a Cartesian coordinate system with the x -axis parallel to the OSNAP line passing through all moorings, the y -axis perpendicular to that line, and the positive z -axis pointing upward. The horizontal resolution of this grid is $\sim 1/4^\circ$ and the vertical resolution is uniformly 20 m.

Mooring data in the boundary arrays are interpolated to estimate the temperature, salinity and density fields in these areas. Away from the arrays, gridded property fields are produced down to 2000 m via an objective analysis method based on temperature and salinity from Argo profiles, OSNAP gliders and moorings, and World Ocean Atlas 2013 (WOA13) temperature (46) and salinity (47) climatology. The WOA13 data are also used in the unmeasured areas on the Labrador and Scottish shelves (Figure 2 of Li *et al.*, 14). Details on the validation of the objective analysis method can be found in previous studies (14, 41). Below 2000 m, hydrographic data from 407 OSNAP CTD stations occupied during the summers of 2014 and 2016 are used to fill the grid. See complete cruise information at <http://www.o-snap.org/observations/research-cruises/>.

Mooring velocity data are interpolated to determine the velocity field in the boundary arrays. Away from the arrays, Ekman velocities calculated using ERA-Interim winds (48) are added to the surface Ekman layer, and geostrophic velocities are calculated with two different choices of reference depending on the availability of deep moorings. Where available, directly measured velocities at the top of deep moorings are used to provide the reference, with two exceptions: one in the western Labrador Basin and one in the central Iceland Basin. There, and in areas without deep moorings, the time-mean surface velocity (over the 21-month observational period) from satellite altimetry is used as the reference velocity. Because of the uncertainties of the surface velocities derived from satellite altimetry in the region (e.g., 49, 50), we use the altimetry-derived velocities to calculate a mean reference velocity only. For each time step, we use this mean reference velocity (only in the areas where we have no direct velocity measurements from moorings) and allow a compensation transport (see below) to determine the time-varying barotropic velocity.

For the unmeasured flow on the Labrador and Scottish shelves (see Figure 2 in Li *et al.*, 14), we use climatological monthly velocities from a high-resolution ($1/12^\circ$) regional ocean general circulation model. The model is the highest resolution member of the Family of Linked Atlantic Modeling Experiments (FLAME) ensemble that was developed for studying circulation in the Atlantic Ocean (34, 51). We repeated our calculations using climatological monthly velocities instead from a high-resolution (7 km) regional ocean-sea ice model (52) for the unmeasured flow above the Labrador shelf. This choice led to MOC, MHT and MFT estimates with negligible differences in the mean and in the variability. Future work includes improved estimates for these inshore properties and velocities.

c. Net throughflow

Our calculation assumes a zero net meridional mass transport across the entire OSNAP section. Long-term measurements across Davis Strait show a mean transport of -1.6 ± 0.2 Sv from the Arctic into the North Atlantic (53). To account for this transport, and still satisfy a zero-net-mass constraint across the entire section, we allow a transport of -1.6 ± 0.2 Sv across OSNAP West and then allow a compensating transport of the same magnitude but opposite sign across OSNAP East. When calculating the MOC at OSNAP West and East separately, we apply these same constraints.

Alternatively, we can require the net throughflow across the entire OSNAP section to be consistent with a recent estimate of 1.0 ± 0.05 Sv entering the Arctic from the Pacific (54) while keeping the 1.6 ± 0.2 Sv southward net transport at OSNAP West. Using these two constraints, we then apply a northward net transport of ~ 0.6 Sv across OSNAP East. As such, there is a mass

imbalance across the entire OSNAP section, matching the Bering Strait throughflow. This added constraint has only a minimal impact on the MOC estimate (14.5 ± 0.9 Sv) compared to a zero-net-throughflow across the entire section (14.9 ± 0.9 Sv). The two time series have a root-mean-square deviation (RMSD) of just 0.5 Sv and are strongly correlated ($r=0.997$). Thus, for this study, we use the zero net meridional mass transport described above, but we continue to explore the best way to account for Pacific to Atlantic throughflows across the entire section, and OSNAP West and East separately.

d. Compensation transport

A compensation transport is added at each time step to ensure a zero net meridional mass transport across the entire OSNAP section (14, 55). That is, we use the constraint of zero net meridional mass transport to identify the fluctuating barotropic component of the flow. The mean compensation transport across the full array and its uncertainty over the observational period is -0.7 ± 3.3 Sv. This mean compensation transport is equivalent to adding a spatially uniform velocity of 0.04 cm/s across OSNAP West and -0.06 cm/s across OSNAP East to those areas without direct velocity measurements. The compensation velocity varies in time: the standard deviation of its time mean is 0.19 cm/s for OSNAP West and 0.44 cm/s for OSNAP East. To test the sensitivity of the MOC estimate to our distribution method, we also applied the compensation velocity uniformly across the whole section, which produced a nearly identical MOC estimate (14.8 ± 0.9 Sv). The two time series are highly correlated ($r=0.99$) and have an RMSD of only 0.7 Sv. While a mean compensation transport of just -0.7 Sv is a strong validation of our methods, we continue to work on retrieving more accurate time-varying barotropic velocities and other ways to reduce this compensation transport and its uncertainty.

e. Mean and uncertainty estimates

We use Monte Carlo simulations to calculate estimates of the mean fluxes and to provide an estimate of the statistical uncertainty in those means. The statistical uncertainty stems from the intrinsic transport variability and random measurement uncertainty, and is typically dominated by the former (56). We note that all reported uncertainties indicate statistical uncertainty, and do not include possible bias errors, i.e., errors due to biases in Ekman transport or to deficiencies in array design or calculation methodology. A possible bias error of up to $\sim 10\%$ of the mean was found in Li *et al.* (14) based on Observing System Simulation Experiments (OSSEs) using a global ocean–sea-ice model. Further analysis will be performed for evaluating possible bias error at OSNAP and its sources.

For each 30-day period: We first create a field of variables used for the MOC, MHT and MFT estimates using the local (i.e., at each instrument site) 30-day mean and standard error for each variable at that site. These variables are temperature, salinity, velocity, sea surface height, wind stress, and the net throughflow across the subsection. For each Monte Carlo iteration, we randomly draw from these distributions to produce one realization of MOC (similarly for MHT and MFT). We continue the Monte Carlo iterations until the running mean of the flux estimate converges to within a prescribed value, ϵ , at which point the standard deviation of the mean has also converged ($\epsilon = 1 \times 10^{-3}$ Sv for MOC, 2×10^{-5} PW for MHT and 2×10^{-5} Sv for MFT). We use the average of all iterations as the mean flux for each 30-day period and report the standard deviation of the average as the uncertainty. Uncertainty in the 30-day mean estimates is ~ 4 Sv for MOC (Fig. 3), 0.1 PW for MHT (Fig. 4) and 0.1 Sv for MFT (Fig. 4).

To calculate the standard error of each variable, we divide the daily standard deviation by $\sqrt{30 \text{ days}/(2\tau)}$, where τ is the integral time scale (days) calculated from the autocorrelation function of the time series (57). We calculate the standard error for each variable at each point on the grid where appropriate. Depending upon the variable and location, τ ranges from a few days to a couple of months.

Over the entire 21-month observational record: To estimate the 21-month mean fluxes, that is the means over the entire observational record, and their uncertainty, we again employ Monte Carlo simulations. For each iteration, we create a 21-month MOC time series from the mean and standard error of each 30-day period, whose calculation is described above. We report the mean and standard deviation of 10,000 Monte Carlo estimates as the final 21-month mean MOC (14.9 Sv) and the corresponding uncertainty (0.9 Sv). The 21-month means and uncertainties for MHT and MFT are similarly obtained.

Alternatively, one can calculate the uncertainty in the 21-month mean as the standard deviation over the entire time period (Table S1) divided by $\sqrt{630 \text{ days}/(2\tau)}$. From the daily MOC time series, τ is estimated as 16 days, which yields 1 degree of freedom for every 32 days. The uncertainty that results from this calculation is 0.9 Sv, identical to that obtained from the Monte Carlo method.

2. Daily MOC estimates

Although daily measurements from all moored instruments are available, the objectively analyzed data product for temperature, salinity and density in the glider domain (see Fig. 2) is generated only every 30 days. The data product in this domain incorporates Argo and glider data, both with insufficient coverage to produce daily estimates. Thus, for our daily time series, we use daily measurements from all moored instruments, yet for the MOC calculation, the same density fields are used over the western flank of the Hatton Bank for each day during each 30-day period. For the MHT and MFT calculations, the same property fields are used in all areas without moored observations for each day during the 30-day period.

To test the extent to which the direct measurements (in the boundary currents) are responsible for the MOC variance at daily time scales, we reran the daily calculation using daily velocities from all moorings, yet we used the 21-month time-mean velocities for areas away from the mooring arrays. This calculation produces a very similar MOC estimate (a 0.7 Sv or ~4% difference) to that produced using time-varying velocities away from the arrays ($r=0.80$ and $\text{RMSD}=3.3$ Sv, using 10-day filtered data for both time series). Thus, we conclude that most of the daily MOC variability occurs in the directly measured boundary currents. Nonetheless, we report the MOC mean and uncertainty based on 30-day estimates, and only show the daily values to indicate the scale of variability on that time scale. We continue to refine the spatial and temporal resolution of the objectively analyzed fields so that in the future we will be able to report OSNAP flux estimates at time scales less than 30 days.

3. Alternative MOC definitions and coordinates

Use of potential density and depth coordinates

For the purpose of this study, the MOC is defined as the maximum of the overturning streamfunction in density space. Alternatively, the MOC can be defined as the maximum of the overturning streamfunction in depth space (maxMOC_z). The MOC using these two definitions is reported in Table S2 and shown in Fig. S1.

Use of neutral density coordinates

We also computed the MOC using neutral density surfaces (58) rather than potential density surfaces and found that the magnitude of the mean estimate was only marginally changed (15.3 ± 0.9 Sv compared to 14.9 ± 0.9 Sv using potential density surfaces; a 3% increase, well within the uncertainty estimate). The variability of the MOC time series created using neutral surfaces is indistinguishable from that using potential density surfaces (i.e., $r = 0.996$).

4. Decomposition of MHT and MFT into overturning and isopycnal components

The MHT and MFT across each OSNAP section are decomposed into overturning and isopycnal components (e.g., 20) by first defining the total velocity, potential temperature and salinity as:

$$v(x, \sigma, t) = \langle v \rangle (\sigma, t) + v'(x, \sigma, t) \quad [m s^{-1}], \quad (S4)$$

$$\theta(x, \sigma, t) = \langle \theta \rangle (\sigma, t) + \theta'(x, \sigma, t) \quad [^{\circ}C], \quad (S5)$$

$$S(x, \sigma, t) = \langle S \rangle (\sigma, t) + S'(x, \sigma, t), \quad (S6)$$

where the angle brackets indicate a horizontal average at constant density and the prime indicates deviations from that average.

The MHT across each OSNAP section can then be divided into an overturning, $MHT_{\text{overturning}}$, and ‘isopycnal’ component, $MHT_{\text{isopycnal}}$, (see Fig. 4) as follows:

$$MHT_{\text{overturning}}(t) = \rho C_P \int_{\sigma_{\min}}^{\sigma_{\max}} \int_{x_w}^{x_e} \langle v \rangle (\sigma, t) \langle \theta \rangle (\sigma, t) dx d\sigma \quad [W], \quad (S7)$$

$$MHT_{\text{isopycnal}}(t) = \rho C_P \int_{\sigma_{\min}}^{\sigma_{\max}} \int_{x_w}^{x_e} v'(x, \sigma, t) \theta'(x, \sigma, t) dx d\sigma \quad [W], \quad (S8)$$

where $\rho C_P = 4.1 \times 10^6 \text{ J m}^{-3} \text{ K}^{-1}$, and the double integral is taken over all σ surfaces and between the western and eastern boundaries.

The MFT across each OSNAP section is similarly decomposed:

$$MFT_{\text{overturning}}(t) = - \int_{\sigma_{\min}}^{\sigma_{\max}} \int_{x_w}^{x_e} \langle v \rangle (\sigma, t) \frac{\langle S \rangle (\sigma, t)}{\bar{S}} dx d\sigma \quad [Sv], \quad (S9)$$

$$MFT_{\text{isopycnal}}(t) = - \int_{\sigma_{\min}}^{\sigma_{\max}} \int_{x_w}^{x_e} v'(x, \sigma, t) \frac{S'(x, \sigma, t)}{\bar{S}} dx d\sigma \quad [Sv]. \quad (S10)$$

The overturning and isopycnal components in density space for both MHT and MFT are shown in Fig. 4. The above decomposition can also be performed in depth space to yield an overturning and horizontal ('gyre') component, both shown in Fig. S2.

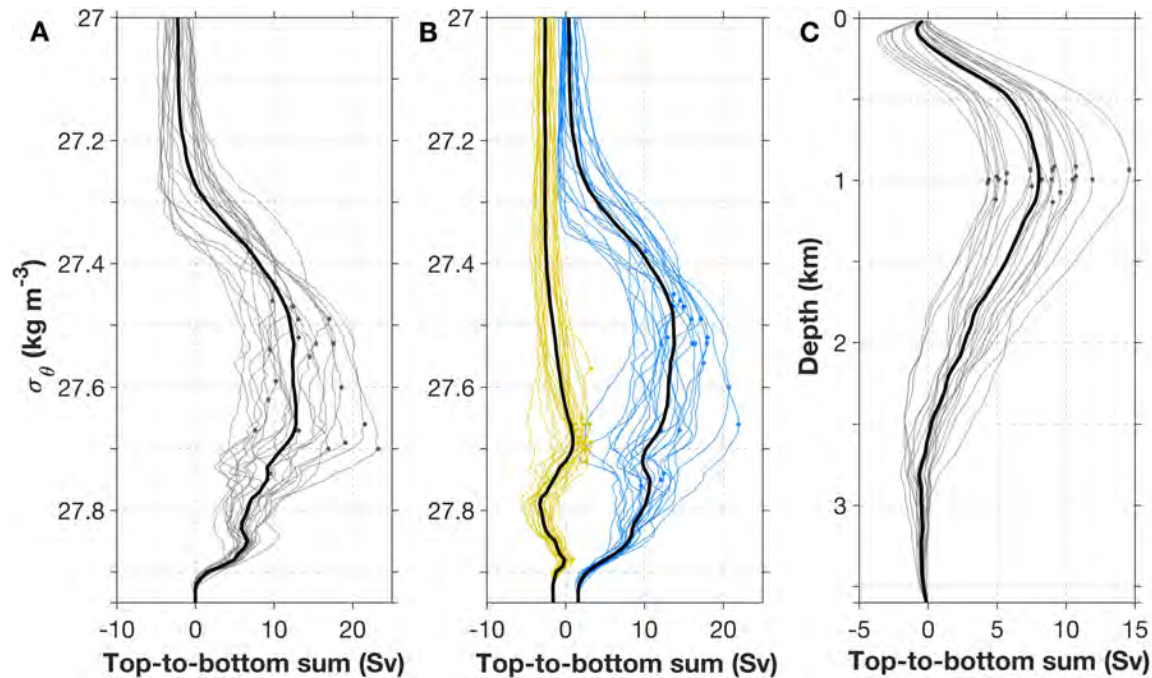


Fig. S1.

Streamfunction across the OSNAP section. Streamfunction in density space across the full array, (A) across the OSNAP West (yellow) and OSNAP East (blue) subsections (B), and in depth space across the full array (C). The 21 30-day means (thin lines) are shown in all panels, with the MOC (maximum of the streamfunction) denoted for each of the 21 profiles (dot). The 21-month mean streamfunction (thick solid lines in all panels) is obtained by averaging all 21 transport values within each density or depth bin. The potential densities corresponding to the maximum of the streamfunction across the subsections (27.69 kg m^{-3} for OSNAP West and 27.53 kg m^{-3} for OSNAP East) are slightly different from that derived from the mean streamfunction across the full array (27.66 kg m^{-3}). The vertical separation between the 27.69 and 27.66 kg m^{-3} isopycnals across OSNAP West is on average less than ~ 100 m, and the separation between the 27.53 and 27.66 kg m^{-3} isopycnals across OSNAP East is on average ~ 100 - 200 m. Note that the maximum value (i.e., the MOC) of the mean streamfunction in density space (thick lines in A and B) underestimates the mean of the 21 individual 30-day MOC estimates reported in the main text. Because the density at which the maxima occur varies over the record, the maximum of the averaged MOC streamfunction will be smaller than an average of the maximum MOC streamfunctions.

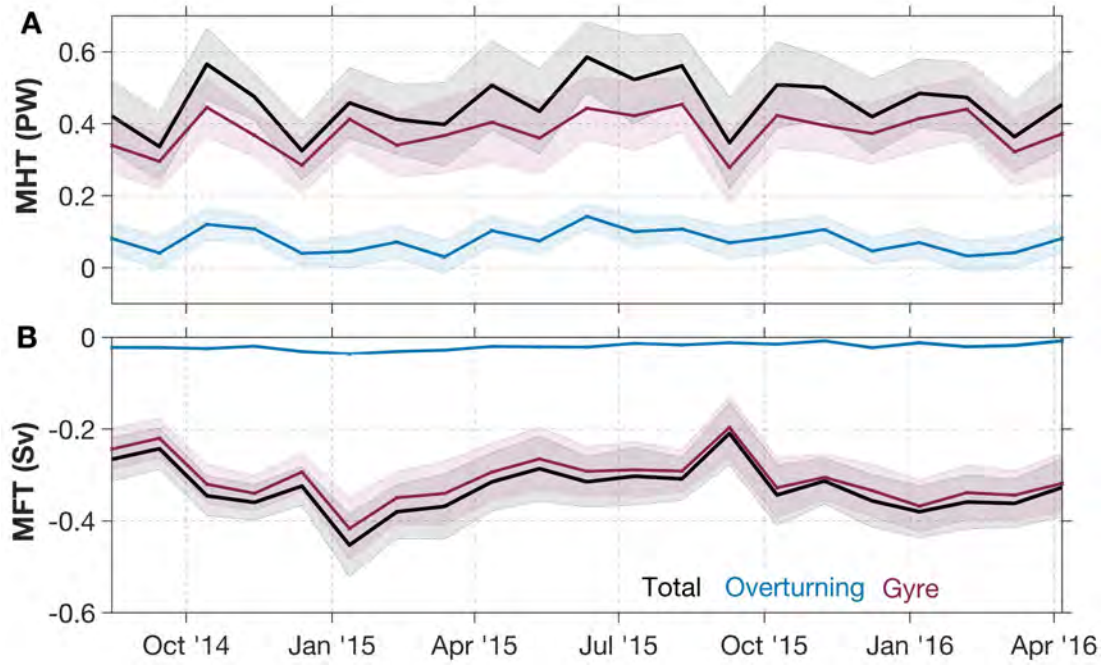


Fig. S2.

MHT and MFT across the OSNAP section. (A and B) Same as in Fig. 4, but with MHT (A) and MFT (B) decomposed in depth space into overturning (blue lines) and gyre (red lines) components.

Table S1.

Mean transport estimates with one standard deviation over the 21-month period. MHT estimates marked with ‘#’ are temperature, rather than heat, transports since there is a net mass flux across these sections. All reported MFT values are equivalent freshwater transports (*14*). The standard deviations here reflect the monthly variability over the 21-month period (Fig. 3), not the uncertainty in the estimate of the mean. For the latter, please see Table S3.

	MOC (Sv)	MHT (PW)	MFT (Sv)
OSNAP	14.9 ± 4.1	0.45 ± 0.08	-0.33 ± 0.05
OSNAP East	15.6 ± 3.1	$0.38^{\#} \pm 0.08$	-0.14 ± 0.04
OSNAP West	2.1 ± 0.9	$0.080^{\#} \pm 0.016$	-0.184 ± 0.041

Table S2.

Comparison of MOC used in text to an alternative definition. The mean MOC and its uncertainty over the period from August 2014 to April 2016 using different MOC definitions and calculated using 30-day means. The first column is the metric used in the text, where MOC is defined as the maximum of the overturning streamfunction in density space (Figs. S1A and S1B). The second column, maxMOC_z , is the maximum of the overturning streamfunction in depth space (Fig. S1C).

	MOC	maxMOC_z
OSNAP	14.9 ± 0.9	8.0 ± 0.7
OSNAP East	15.6 ± 0.8	8.2 ± 0.6
OSNAP West	2.1 ± 0.3	0.8 ± 0.2

Table S3.**Compilation of MOC, MHT, MFT and Ekman transport estimates in the North Atlantic.**

Reported values are the time mean plus/minus an uncertainty estimate. MOC estimates marked with ‘*’ are those calculated in depth space; otherwise, density space is used. MHT estimates marked with ‘#’ are temperature, rather than heat, transports since there is a net mass flux across these sections. All reported MFT values are equivalent freshwater transports (14). Estimates are based on direct measurements from different time periods. The long-term mean RAPID-MOCHA MOC (M15a: 26), MHT (26), MFT (M15b: 59) and Ekman transport (M15a) are for April 2004 – October 2012, while the latest estimate of the MOC and Ekman transport during the overlap period with OSNAP are for 2014 – 2016 (S18: 21). The uncertainties marked with ‘&’ are calculated based on the reported uncertainties in the annual volume (0.9 Sv; M15a) and freshwater (0.02 Sv; M15b) transports. The OVIDE MOC estimate is for 1993 – 2010, while the OVIDE MHT is the mean summer estimate between 1997–2010 (22). There are two MOC estimates at 59.5°N: one is the 2002-2008 mean summer estimate (S12: 29), the other is the long-term mean estimate between early 2012 to early 2016 (R17: 30). The latter study also provided MHT and MFT estimates. The MOC estimated at AR7W is based on either repeat hydrography between 1990-1997 (P07: 25) or Argo floats between March 2002 – April 2016 (H17: 28).

	MOC (Sv)	MHT (PW)	MFT (Sv)	Ekman (Sv)
OSNAP	14.9 ± 0.9	0.45 ± 0.02	-0.33 ± 0.01	-1.72 ± 0.02
RAPID-MOCHA	17.2* ± 0.3& (M15a)	1.25 ± 0.11 (M15a)	-0.43 ± 0.007& (M15b)	3.8 (M15a)
	16.8* ± 0.5& (S18)			3.9 (S18)
OSNAP East	15.6 ± 0.8	0.38# ± 0.02	-0.14 ± 0.01	-1.51 ± 0.02
OVIDE	18.1 ± 1.4	0.51# ± 0.06		
59.5°N	18.4 ± 3.4 (R17)	0.399# ± 0.074	-0.20 ± 0.04 (R17)	
	16.6 ± 1.1 (S12)	(R17)		
OSNAP West	2.1 ± 0.3	0.080# ± 0.004	-0.184 ± 0.004	-0.18 ± 0.01
AR7W	2 (P07)	0.038 (P07)		
	1* (P07)			
	2.5 ± 0.75 (H17)			
	0.9* ± 0.5 (H17)			

References and Notes:

46. R. A. Locarnini *et al.*, "World Ocean Atlas 2013, Volume 1: Temperature," (NOAA Atlas NESDIS 73, 2013).
47. M. M. Zweng *et al.*, "World Ocean Atlas 2013, Volume 2: Salinity," (NOAA Atlas NESDIS 74, 2013).
48. D. P. Dee *et al.*, The ERA-Interim reanalysis: configuration and performance of the data assimilation system. *Quart. J. Roy. Meteor. Soc.* **137**, 553-597 (2011).
49. C. Gourcuff, P. Lherminier, H. Mercier, P. Y. Le Traon, Altimetry combined with hydrography for ocean transport estimation. *J. Atmos. Oceanic Technol.* **28**, 1324-1337 (2011).
50. T. J. Sherwin, D. Aleynik, E. Dumont, M. E. Inall, Deep drivers of mesoscale circulation in the central Rockall Trough. *Ocean Sci.* **11**, 343-359 (2015).
51. C. W. Böning, M. Scheinert, J. Dengg, A. Biastoch, A. Funk, Decadal variability of subpolar gyre transport and its reverberation in the North Atlantic overturning. *Geophys. Res. Lett.* **33**, L21S01 (2006).
52. G. Han, Z. Ma, Z. Long, W. Perrie, J. Chassé, Climate change on Newfoundland and Labrador shelves: Results from a regional downscaled ocean and sea-ice model under an A1B forcing scenario 2011–2069. *Atmo.-Ocean*, 1-15 (2018).
53. B. Curry, C. M. Lee, B. Petrie, R. E. Moritz, R. Kwok, Multiyear volume, liquid freshwater, and sea ice transports through Davis Strait, 2004-10*. *J. Phys. Oceanogr.* **44**, 1244-1266 (2014).
54. R. A. Woodgate, Increases in the Pacific inflow to the Arctic from 1990 to 2015, and insights into seasonal trends and driving mechanisms from year-round Bering Strait mooring data. *Prog. Oceanogr.* **160**, 124-154 (2018).
55. M. M. Hall, H. L. Bryden, Direct estimates and mechanisms of ocean heat-transport. *Deep-Sea Res. I* **29**, 339-359 (1982).
56. W. E. Johns *et al.*, Continuous, Array-based estimates of Atlantic Ocean heat transport at 26.5°N. *J. Climate* **24**, 2429-2449 (2011).
57. R. E. Thomson, W. J. Emery, "Time-series Analysis Methods" in *Data Analysis Methods in Physical Oceanography*, R. E. Thomson, W. J. Emery, Eds. (Elsevier Science, 2014), chap. 5, pp. 432.
58. D. R. Jackett, T. J. McDougall, A neutral density variable for the world's oceans. *J. Phys. Oceanogr.* **27**, 237-263 (1997).
59. E. L. McDonagh *et al.*, Continuous estimate of Atlantic oceanic freshwater flux at 26.5°N. *J. Climate* **28**, 8888-8906 (2015).